Solder Joint Geometry Effects on Thermomechanical Fatigue Lifetime of End-Capped Chip Component Assemblies

Vincent Voet, Christophe De Fruytier, Thomas Pardoen, and Aude Simar

***Abstract*— Electronic component assemblies are exposed to thermal cycles that lead to the thermomechanical fatigue of the solder joints. The effect of the joint geometry on the fatigue lifetime of the assembly is investigated for rectangular end-capped chip components in order to both increase the predictive capabilities of integrity assessment schemes and to guide toward more durable designs. A two-step approach is developed including two models considering the region of the joint underneath the component and the filet, respectively. Local values of the inelastic strain energy density are extracted from finite element (FE) simulations. Phenomenological failure power-law models are identified based on experimental data and previously developed cohesive zone model (CZM) describing the fatigue cracking process. The analysis proves that the filet and its shape play a primary role in setting the fatigue lifetime of the solder layer.**

***Index Terms*— Accelerated thermal cycling, finite element (FE) analysis, soldering, thermomechanical fatigue.**

I. Introduction

ELECTRONIC assemblies, comprised of many electronic components soldered on printed circuit boards (PCBs), are part of a tremendous number of equipment used in everyday life and in industry. High-reliability applications such as space devices require a deep understanding of fatigue resistance and consistent lifetime assessment capabilities. During operation, electronic equipment are exposed to various thermal cycles, leading to cyclic deformation and hence thermomechanical fatigue of the joint due to the mismatch of the coefficients of thermal expansion of the constitutive materials, i.e., component, solder joint, and PCB [1], [2], [3], [4]. Many factors influence the reliability including the component type, size and material, PCB build-up and material, solder joint volume, shape and material and mounting process.

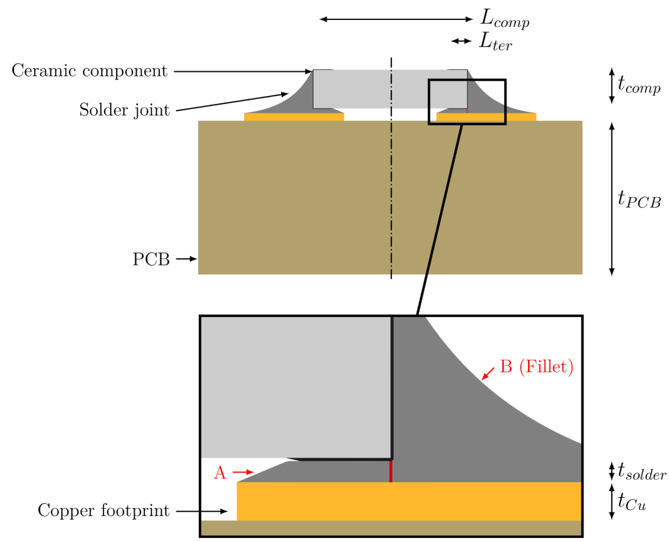

Fig. 1. End-capped chip component assembly geometric configuration, showing constitutive elements, lengths, and both solder joint regions A and B, underneath the component and the filet, respectively.

This research work focuses on rectangular end-capped chip components (e.g., resistors) as shown in Fig. 1, although the methodology is general and can be directly transposed to other geometries. The various parts include the ceramic component, its termination (i.e., the layer in contact with the joint), the solder joint, the copper footprint, and the PCB. Two regions of the joint are defined: region A, underneath the component, and region B, the filet. Fig. 2 presents a micrograph of a failed component with a crack that started propagating in region A and continued growing into region B. Failure of solder joint assemblies can be defined either as corresponding to the cracking of the region underneath the component [5], or as corresponding to the cracking of the entire joint, including the filet region. Each choice can be justified by the use of a standardized method or depending on the application. Experimental failure can be physically related to crack lengths directly measured on micro sections, which provide a view of the whole surface of the joint at a given cross section plane for a given number of thermal

Manuscript received 28 March 2023; revised 10 August 2023; accepted 18 December 2023. Date of publication 5 January 2024; date of current version 27 February 2024. This work was supported by the Service Public de Wallonie-Wallonie recherche through the project "Stress". Recommended for publication by Associate Editor L. Aryasomayajula upon evaluation of reviewers' comments. *(Corresponding author: Vincent Voet.)*

Vincent Voet is with the Institute of Mechanics, Materials and Civil Engineering, IMAP, UCLouvain, 1348 Louvain-la-Neuve, Belgium, and also with Thales Alenia Space Belgium, 6032 Mont-sur-Marchienne, Belgium (e-mail: vincent.voet@uclouvain.be).

Christophe De Fruytier is with Thales Alenia Space Belgium, 6032 Mont-sur-Marchienne, Belgium.

Thomas Pardoen and Aude Simar are with the Institute of Mechanics, Materials and Civil Engineering, IMAP, UCLouvain, 1348 Louvain-la-Neuve, Belgium.

Color versions of one or more figures in this article are available at https://doi.org/10.1109/TCPMT.2024.3350184.

Digital Object Identifier 10.1109/TCPMT.2024.3350184

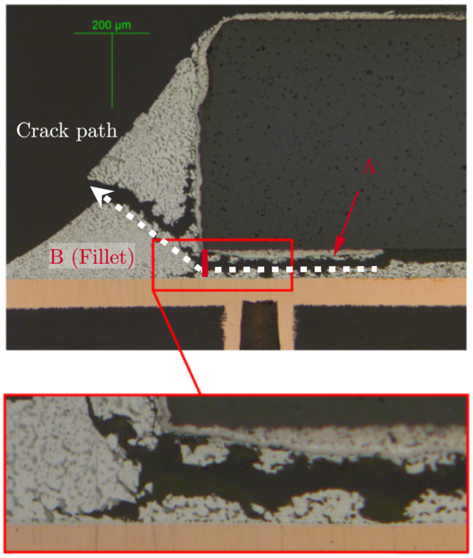

Fig. 2. Micrograph of a failed solder joint with a crack that propagated through regions A and B (i.e., the filet).

cycles or based on electrical monitoring. The latter consists of continuous electrical resistance measurements of assembled components. Failure is reported once a defined drift in the resistance is attained. A Weibull plot can be extracted from raw data. Failure can also be predicted by finite element (FE) simulations based on different damage indicators, such as a critical inelastic strain or a critical inelastic strain energy density [3], [6], [7].

The effect of the solder joint geometry on the fatigue lifetime of the assembly has been studied by Liu and Lu [8] on ball grid array (BGA) components. They highlighted a significant effect of the ball shape and height on the number of cycles to failure. Other studies have also confirmed that these parameters are indeed important [9], [10], [11]. Various solder paste volumes and hence solder joint shapes were simulated by Wang et al. [12] for chip resistors. They predicted a significant increase in lifetime for larger filet configurations. Slightly concave shapes showed the highest number of cycles to failure according to Zheng and Wang [13]. Highly convex filet shapes had a shorter fatigue lifetime. Jih and Pao [14] used the total shear strain range, $\Delta\gamma$, as a failure criterion to compare various component and solder joint geometries. They calculated an increase in the shear strain range for increasing component sizes and a decrease of $\Delta\gamma$ for thicker joints. The filet shape was found to have little effect on the shear strain range. The change of $\Delta\gamma$ was also relatively small for various filet heights and lengths.

The focus of a previous study [5] made in the context of this research was on the failure of region A only. In addition to setting an original methodology based on machine learning processed experimental data and crack propagation FE simulations of the fatigue process, this study showed that several parameters, such as the solder joint thickness or component length and thickness, significantly influence the fatigue lifetime of the assembly. However, as explained above, the failure in the filet region was not taken into account. The objective of the present study is to compare the contribution of each region (A and B) on the predicted fatigue lifetime and to assess how the filet geometry influences the damage resistance. The final goal is to provide a better understanding of the joint fatigue behavior and to open new opportunities to improve assembly design.

Section II introduces the methods and the models developed to estimate the lifetime of the solder joint in regions A and B (see Fig. 1). The FE model is described first with the material's behavior and loading conditions. The models are identified and validated by experimental data. A discussion related to the damage criterion is held.

Section III presents some applications of the models by comparing different filet configurations and each region's contribution to the fatigue lifetime of a selection of assemblies. It includes the effect of the solder joint thickness and the component size. The results obtained with the model are compared to the predictions made with the Norris–Landzberg's (N-L) aging law.

II. Methods and Models

Two models are developed in this article: the first predicts fatigue failure in the region underneath the component (region A) only and the second, the failure of the filet (region B). The first subsection introduces the FE model, the second focuses on region A and the third on region B. For the various component sizes that will be exploited in the article, the model considers both the length and thickness (L_{comp} and t_{comp} in Fig. 1) to parameterize the geometry. The commercial FE software Abaqus is used with the implicit solver.

A. FE Model

The component is a surface-mounted ceramic resistor with nickel terminations mounted on a copper footprint, part of a PCB as shown in Fig. 1. The ceramic body is made of alumina (Al_2O_3). The PCB material is polyimide Arlon 35N [15]. The solder alloy is Sn62 (62% of tin, 36% of lead, and 2% of silver). Two-dimensional plane strain conditions are imposed, justified by the fact that the out-of-plane width is much larger than the thickness of the layers undergoing the failure process. It brings in a small bias on the calculated values. The FE mesh is presented in Fig. 3. A zoom on the region underneath the component is also provided.

All materials are considered thermally isotropic with a coefficient of thermal expansion α. Linear elastic isotropic behavior is assumed for all materials with Young's modulus E and Poisson ratio ν, via Hooke's law. Plastic deformation is allowed in both nickel and copper materials relying on the experimental data from Jenkins et al. [16] and modeled using J_2 flow theory. The temperature-dependent viscoplastic behavior of the solder alloy is described using Anand's model [17]

$$\dot{\epsilon}^p = A \exp\left(\frac{-Q}{RT}\right)\left[\sinh\left(\xi\frac{\sigma}{s}\right)\right]^{1/m} \tag{1}$$

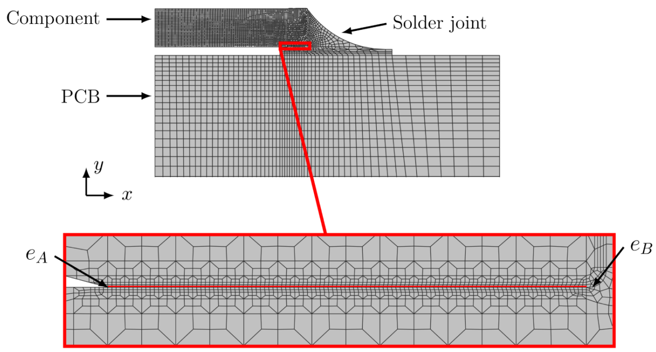

Fig. 3. Mesh of the FE model with a magnification of the interface between the component and the solder joint in region A. The location of the regions used to calculate the inelastic strain energy density in region A, e_A, and in region B, e_B are shown. Simulations in region B are conducted with a pre-crack underneath the component highlighted in red.

where

- $\dot{\epsilon}^p$ inelastic strain rate;
- A material constant;
- ξ stress multiplier;
- m strain rate sensitivity;
- Q activation energy;
- R ideal gas constant;
- s deformation resistance which is computed via an evolution law

$$\dot{s} = h_0\left|1 - \frac{s}{s^*}\right|^a \mathrm{sign}\left(1 - \frac{s}{s^*}\right)\dot{\epsilon}^p \tag{2}$$

where

- h_0 hardening constant;
- a hardening strain rate sensitivity;
- s^* saturation value of s, which writes

$$s^* = \hat{s}\left[\frac{\dot{\epsilon}^p}{A}\exp\left(\frac{Q}{RT}\right)\right]^n \tag{3}$$

where

- $\hat{s}$ coefficient of the saturation of the deformation resistance;
- n strain rate sensitivity of the saturation of the deformation resistance.

The initial value of the deformation resistance, s_0, is also a material parameter. Tables I and II list the values of the material parameters extracted from literature [3], [18], [19], [20], [21]. The Young's modulus and reference stress values are normalized by the initial yield stress of the solder joint σ_{y0}, equal to 28 MPa (at 20 °C and at an inelastic strain rate of $5 \cdot 10^{-4}$ [s^{-1}]), calculated from Anand's model parameters [18]. As suggested by Basaran and Jiang [22], Young's modulus of the solder alloy has been measured by nano-indentation on an actual manufactured sample, confirming the value of 42 GPa (at 25 °C) computed from the temperature-dependent equation in Table I. The component assembly is exposed to thermal cycles. The temperature is imposed to be uniform within the model owing to the small size of the component. Note that the model is sensitive to time [see (1)] and thus to the rate of change of the temperature.

TABLE I

ELASTIC PROPERTIES AND COEFFICIENTS OF THERMAL EXPANSION, FROM [3], [19], [20], [21]

Material	E [GPa]	E/σ_{y0} [−]	ν [−]	α [10^{-6}·°C^{-1}]
Alumina ceramic	410	14 640	0.25	5.5
Nickel	180	6430	0.31	13
Solder	62 − 0.067·T	2214 − 2.39·T	0.35	27
Copper	120	4290	0.35	17
Polyimide PCB	27	964	0.3	15.5

TABLE II

VALUES OF ANAND'S PARAMETERS FOR 62Sn36Pb2Ag SOLDER ALLOY, ACCORDING TO DARVEAUX [18]

Material parameter	value	dimensionless value [−]
A	$4 \cdot 10^6$ [s^{-1}]	-
Q/R	9400 [K]	-
ξ	1.5 [-]	-
m	0.303 [-]	-
h_0	1379 [MPa]	49.25
a	1.3 [-]	-
$\hat{s}$	13.79 [MPa]	0.4925
n	0.07 [-]	-
s_0	12.41 [MPa]	0.4432

B. Methodology for Modeling Failure in Region A

A machine learning-aided FE modeling approach has been previously developed in region A by Voet et al. [5]. The main concept and useful results are exploited here; the workflow is presented in Fig. 4. The investigation started from micro sections of electronic assemblies at a given number of thermal cycles (500 cycles between −55 °C and 100 °C at 10 °C/min and 15 min dwell times). Important parameters were then selected and compiled into a database which was used to train and test a machine learning (fully connected neural network) model. The latter allowed the identification and validation of the cohesive zone FE model.

Static analysis with the inelastic strain as a failure criterion was compared to the crack propagation analysis, showing similar trends [5]. Another criterion, the inelastic strain energy was assessed and compared to the inelastic strain criterion and crack propagation analysis. The inelastic strain energy is calculated based on a volume e_A as shown in Fig. 3. The mesh near this element is not changed in the different simulations. Three thermal cycles are simulated and the considered increment of $\epsilon_{\mathrm{eq}}^{\mathrm{in}}$ and W^{in} per cycle is recorded during the third cycle. The comparison is presented in Fig. 5. Both static simulation damage criteria are in agreement with crack propagation analysis, except for a very thick joint configuration[1] (orange square at W^{in}/cycle = 1.5) where the inelastic strain energy was out of the overall trend (i.e., higher than the inelastic strain). The values are normalized by the default test configuration (see [5, Table IV]).

However, further analysis indicated that the inelastic strain criterion does not capture the trend for several specific loading conditions such as increasing/decreasing temperature ramp rate as illustrated in Fig. 6. Indeed, for a lower ramp rate, $\epsilon_{\mathrm{eq}}^{\mathrm{in}}$ increases whereas W^{in} decreases. Experimental data gath-

[1]Such a thick joint configuration is not considered any further in the following.

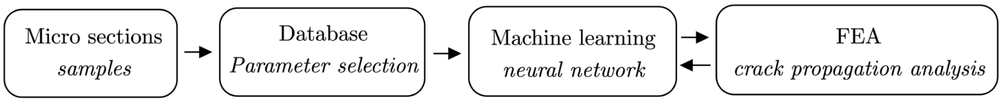

Fig. 4. Workflow of the approach built to identify and validate the crack propagation model in region A.

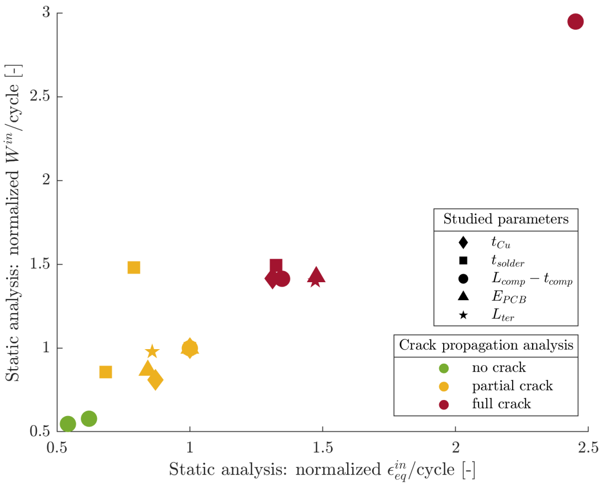

Fig. 5. Comparison between the equivalent inelastic strain and the inelastic strain energy accumulated per cycle while also indicating the cracking status in the region underneath the component for various parametric study configurations, extracted from [5]. Both static simulation damage criteria are normalized by the values obtained for the default configuration tested.

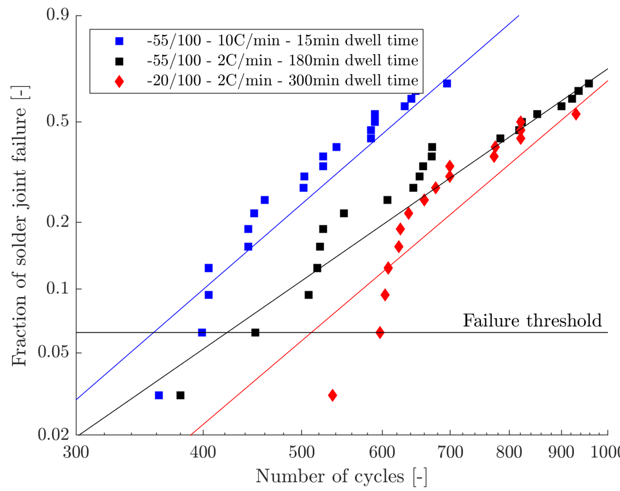

Fig. 7. Experimental fraction of solder joint failure for 2512 chip resistors from Thales Alenia Space. The data consists of electrical continuity monitoring, considering failure in both A and B regions. Three temperature cycles are compared as described in the legend. The failure threshold used to identify the power law in region B (see Fig. 10) is indicated.

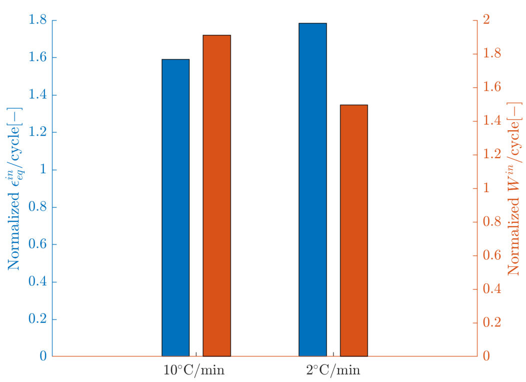

Fig. 6. Comparison between RM2512[2] static simulation damage criteria ($\epsilon_{\text{eq}}^{\text{in}}$ and W^{in}) for two temperature ramp rates (with a temperature cycle between −55 °C and 100 °C).

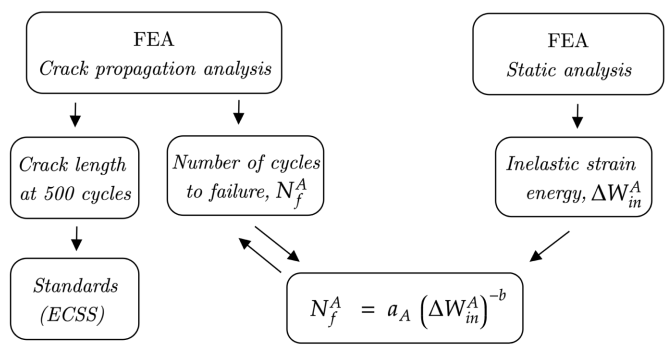

Fig. 8. Strategy for the identification of the power law parameters a_A and b in region A.

ered by Thales Alenia Space, see Fig. 7, shows delayed failure for a lower ramp rate; see blue and black squares at 10 °C/min and 2 °C/min ramp rates, respectively. The thermal cycle dwell time is also increased, but is expected to reduce the lifetime of the assembly [23], [24], which further emphasizes the ramp rate effect. The inelastic strain energy criterion provides better prediction trends in this case which justifies the choice of that specific failure criterion in what follows.

The way thermal cycle properties affect the reliability of the assembly is not necessarily obvious or systematic. Qi et al. [25] tested experimentally two temperature ramp rates for RM2512 resistors, at 14 °C/min and 95 °C/min and between 0 and 100 °C. They measured a slightly better reliability for the highest ramp rate but this was not observed in all test samples. They concluded that the ramp rate has little effect on failure. Ghaffarian [26] studied the fatigue reliability by applying ramp rates of 2 °C/min to 5 °C/min and 10 °C/min to 15 °C/min on BGA packages and showed a strong decrease in the fatigue lifetime for the highest cooling/heating rates. Wu et al. [27] investigated ramp rate effects on solder balls as well. They found a decrease in the fatigue lifetime for increasing temperature ramp rates. Increasing the dwell time has a larger impact than the temperature ramp rate on BGA solder joint reliability according to Zhai et al. [28]. Clech [23] pointed out that at a high temperature (i.e., 100 °C), the dwell time has little effect due to stress relaxation, although a decrease of the fatigue lifetime is noticed for an increasing

[2]The component nomenclature is as follows: the first two figures indicate the component length and the last two, the component width, both expressed in hundredths of inches.

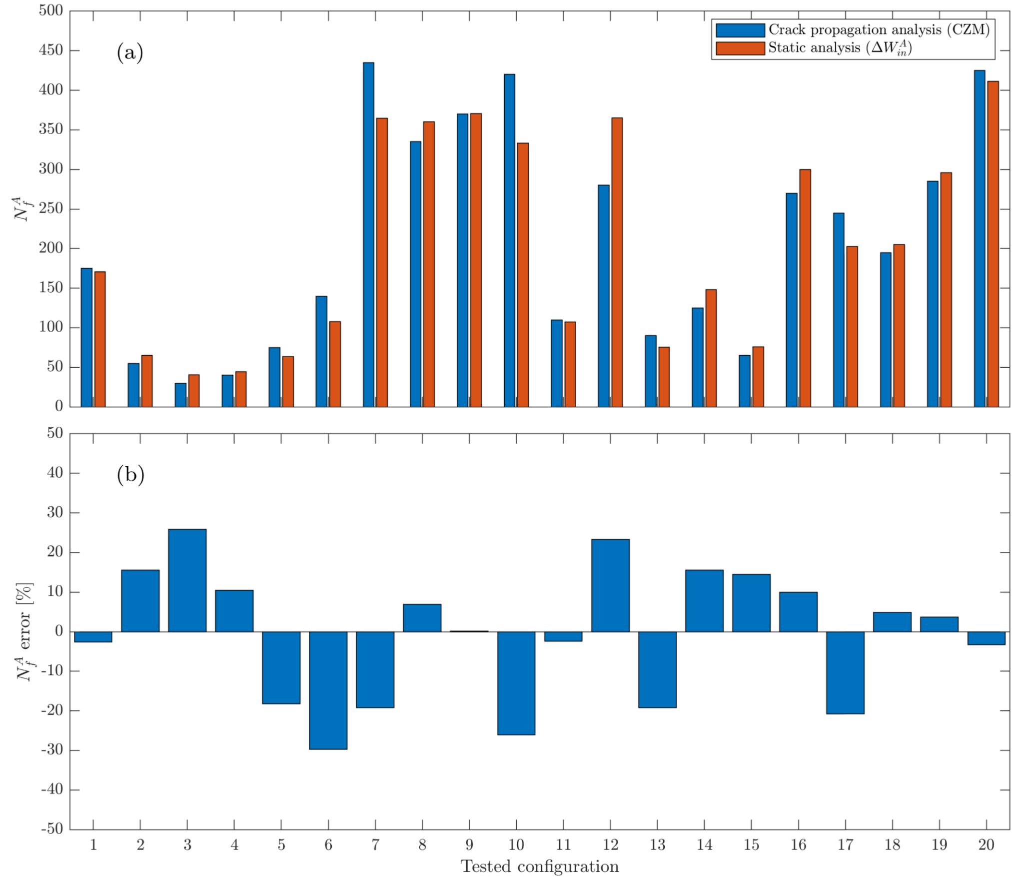

Fig. 9. Comparison between the CZM predictions and the phenomenological model in region A. (a) Twenty samples are tested with a wide variety of configurations. (b) Model prediction errors.

cold temperature dwell time. Hung et al. [24] tested two dwell times of 30 and 66 min on power module assemblies. The longer cycle period showed an earlier crack initiation and a larger growth rate. In Fig. 7, the longer period cycle has an increased fatigue lifetime whereas it has longer dwell times but also lower ramp rates. This indicates that it is complex to deliver definitive conclusions on the effect of accelerated thermal cycle parameters. Indeed, a number of additional factors affect these trends such as the type of component, joining process, PCB configuration, and test conditions.

A phenomenological failure power law can now be established to evaluate the number of cycles to failure (in region A) based on the inelastic strain energy criterion, $N_f^A = a_A(\Delta W_{\text{in}}^A)^{-b}$. The parameters are defined in Fig. 8. The latter also presents the overall failure assessment strategy followed in region A.

The main two outcomes of the crack propagation analysis are the determination of the crack length at a given number of cycles, which is of major interest for ESA standards (ECSS-Q-ST-70-61C [29]), and the number of cycles to failure, N_f^A, as used here. Static FE simulations with the inelastic strain energy criterion are conducted. The two parameters, a_A and b, of the power law are identified and assessed thanks to the crack propagation analysis. The exponent, b, was found to be around 5/3 by the least square method. Many power law models based on either the inelastic strain or the strain energy density and with or without improvements such as frequency-modified models [30] have been developed in the literature [31], [32]. The fatigue exponent is usually within the range 1 to 1.6 [6], [30], [33], [34]. The b exponent estimated here is in the high range. The parameter a_A depends on the volume over which the energy density is averaged and possibly also on the mesh. Therefore, it is challenging to compare values with literature data. For the modeling conditions used in this study, the value of a_A was found to be around $3.2 \cdot 10^{-4}$ [−].

Fig. 9(a) presents a comparison between the crack propagation analysis using a cohesive zone model (CZM) and the predictions based on the inelastic strain energy criterion (ΔW_{in}^A). Many configurations are assessed, including various component lengths, L_{comp}, thicknesses, t_{comp}, termination lengths, L_{ter}, copper footprint thicknesses, t_{Cu}, PCB stiffnesses, E_{PCB}, solder joint thicknesses, t_{solder} and loading conditions (including temperature ramp rate, $\dot{T}$, temperature range, ΔT, mean temperature, $\bar{T}$ and dwell time, t_{dwell}). The range of the tested parameters is available in Table III. The lengths are normalized by the PCB thickness and are defined in Fig. 1. The trends captured by the phenomenological model are clearly in line with the CZM predictions.

Relative errors between the CZM predictions and the inelastic strain energy criterion are shown in Fig. 9(b). The errors are within the range of plus or minus 30%, leading to acceptable

TABLE III
RANGE OF PARAMETERS TESTED IN REGION A

Parameter	L_{comp}/t_{PCB}	t_{comp}/t_{PCB}	t_{solder}/t_{PCB}	L_{ter}/t_{PCB}	t_{Cu}/t_{PCB}
Range [-]	0.8 - 2.6	0.2 - 0.3	0.004 - 0.015	0.08 - 0.13	0.008 - 0.04
Parameter	E_{PCB}/E_{solder}	$\dot{T}$	ΔT	$\bar{T}$	t_{dwell}
Range [-]	0.64 - 2	2 - 10 [°C/min]	120 - 155 [°C]	22.5 - 40 [°C]	15 - 300 [min]

TABLE IV
RANGE OF PARAMETERS TESTED IN REGION B

Parameter	L_{comp}/t_{PCB}	t_{comp}/t_{PCB}	t_{solder}/t_{PCB}	L_{ter}/t_{PCB}	t_{Cu}/t_{PCB}
Range [-]	2.1 - 2.6	0.25 - 0.3	0.015	0.13	0.04
Parameter	E_{PCB}/E_{solder}	$\dot{T}$	ΔT	$\bar{T}$	t_{dwell}
Range [-]	0.64 - 0.95	2 - 10 [°C/min]	120 - 155 [°C]	22.5 - 40 [°C]	15 - 300 [min]

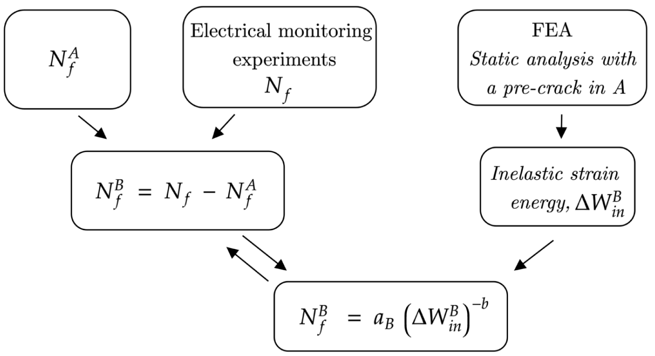

Fig. 10. Strategy for the identification of the power law parameter a_B in region B.

predictability capabilities. At this point, a simple phenomenological failure model has been identified and validated thanks to advanced crack propagation simulations themselves identified and validated by a machine learning model trained and tested on a database based on micro sections acquired during qualification campaigns by Thales Alenia Space.

C. Methodology for Modeling Failure in Region B

A similar approach, including the inelastic strain energy as a failure criterion, is used to estimate the fatigue lifetime in region B, see Fig. 10. The strain energy is calculated based on a volume e_B as shown in Fig. 3. Simulations are conducted with a pre-crack underneath the component such that region A is considered completely failed once region B starts to damage. This is based on experimental observations. The experimental number of cycles to complete failure in regions A and B, N_f, is obtained from electrical monitoring tests. This allows estimating the number of cycles to failure in region B, N_f^B from the number of cycles to failure calculated in Section II-B, N_f^A. A failure power law model is identified, based on N_f^B and ΔW_{in}^B. The exponent b is kept constant from the failure model in region A.

The number of available electrical monitoring data is limited; only five configurations are tested. This is mainly due to the time required to carry out the thermal cycling tests (usually at least several months). It also justifies the use of a small fraction of failed solder joints during the tests instead of a higher failure percentage [not enough data was available for the first two configurations presented in Fig. 11(a)]. A fraction of 6% has been selected, establishing the number of cycles to failure, $N_f^{6\%}$, see Fig. 7. The range of test configurations is provided in Table IV. A first evaluation of the power law predictions is shown in Fig. 11(a), showing poor agreement with the experimental (electrical monitoring tests) results and the number of cycles to failure in region A. Nevertheless, some trends are well predicted; an increase in the fatigue lifetime is observed when comparing configurations 1 and 2, 3 and 4, and 4 and 5. As a matter of fact, these experiments come from two different campaigns (and two assembly lines) and only some of the parameters have been considered by the numerical simulations due to the lack of data or due to noncontrollable parameters.

The data is now separated into two groups, corresponding to the two test campaigns; the first includes configurations 1 and 2 and the second, from 3 to 5. The predictions are much more reliable, as shown in Fig. 11(b). But, still, some under and overestimations are noticed for configurations 3 and 5, respectively. The blue, the black, and the red curves of Fig. 7 correspond to configurations 3, 4, and 5, respectively. Experimental results for configuration 5 do not follow expectations; by decreasing the temperature range and especially increasing the cold temperature, a significant improvement in the fatigue lifetime should be noticed, even with the longer dwell times. The predicted increase between configurations 3 and 4 is also higher than the measured one but is explained by the choice of a $N_f^{6\%}$. A larger failure threshold would have increased this experimental trend. The value of a_B was found to be around $3.2 \cdot 10^{-2}$ [−].

III. Exploitation of the Models

The two previously described models can be used to estimate the number of cycles to failure for some typical configurations, such as several filet geometries, solder joint thicknesses, and component sizes. Another temperature cycle is simulated and compared to N-L aging law predictions.

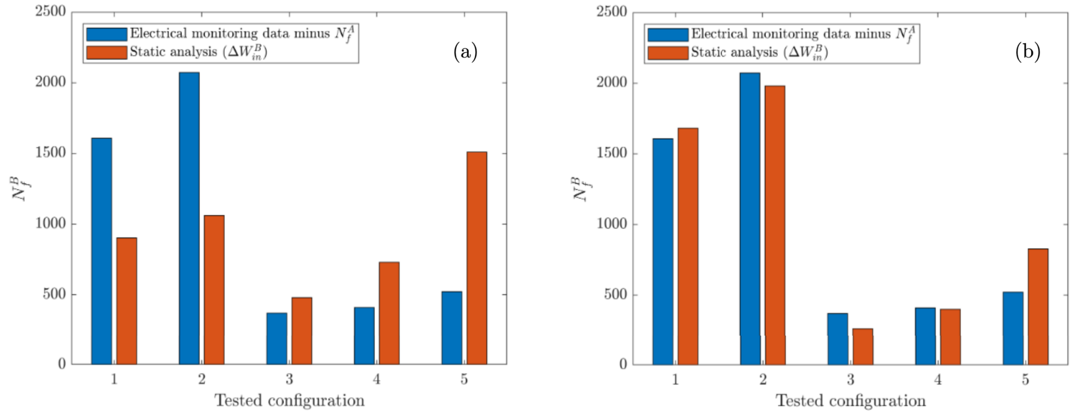

Fig. 11. Comparison between the experimental electrical monitoring data minus N_f^A and the phenomenological power law failure model with the inelastic strain energy in region B. Five samples are tested with various configurations. (a) Includes each configuration without distinction and (b) considers the two test campaigns independently (configurations 1 and 2 and from 3 to 5).

TABLE V
DEFAULT PARAMETERS FOR THE EXPLOITATION OF THE MODELS

Parameter	L_{comp}/t_{PCB}	t_{comp}/t_{PCB}	t_{solder}/t_{PCB}	L_{ter}/t_{PCB}	t_{Cu}/t_{PCB}
Value [-]	2.1	0.25	0.015	0.13	0.04
Parameter	E_{PCB}/E_{solder}	$\dot{T}$	ΔT	$\bar{T}$	t_{dwell}
Value [-]	0.64	10 [°C/min]	155 [°C]	22.5 [°C]	15 [min]

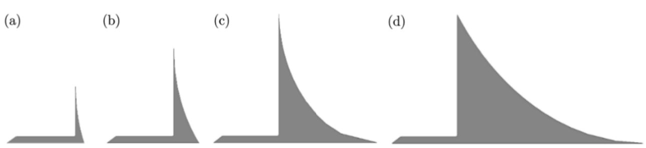

Configuration	a	b	c	d
V_{fillet}/V_{joint} [%]	30	65	90	95

Fig. 12. Solder joint filet configurations simulated, from (a) very small and thin to (d) extended filet. For the sake of readability, only the solder joint is presented, the assembly is described in Fig. 1. The ratio between the volume of the filet and the entire volume of the joint is also indicated.

Static FE simulations with the inelastic strain energy as a failure criterion are conducted and the number of cycles to failure are calculated thanks to the identified phenomenological power laws. Default parameters used in this section are provided in Table V.

A. Filet Geometry Effect

Four filet geometries are compared and presented in Fig. 12, from a small and thin joint filet to an extended filet configuration. The FE models developed for regions A and B are used to estimate the fatigue lifetime of the joints. The filet-to-joint volume ratio, i.e., the ratio between the joint filet volume, V_{filet}, and the joint's entire volume, V_{joint}, for each of the configuration is also provided in Fig. 12. In configuration (a), 70% of the solder material is located underneath the component whereas it only represents 5% in configuration (d).

Fig. 2 showed a crack in a failed component's solder joint. It had propagated through region A and through the filet, leading to the total failure of the joint. The fillet's shape and volume are key parameters for the fatigue lifetime of the assembly. The longer the distance required for a crack to propagate, the longer the number of cycles to failure.

Static simulations without and with a pre-crack underneath the component, i.e., in region A, are conducted. The inelastic strain energy is extracted in order to determine the number of cycles to failure, N_f. Fig. 13 shows the estimated lifetime of the solder joint. Blue bars represent the number of cycles to failure in region A and red bars correspond to region B. There is a significant impact of the filet geometry on the number of cycles to failure between the four configurations, even more for (a), (b), and (c). This effect is certainly underestimated due to the much longer distance that has to be cracked to reach complete failure in the filet for larger filet configurations. It is clear that the number of cycles to failure in configuration (d) will be significantly larger than in configuration (c) but as the volume used to average the inelastic strain energy is fixed, the model cannot capture this trend.

Experimental observations have been made based on two solder joint geometries imposed by the PCB copper footprint design. Fig. 14 presents the two filet geometries. The "optimum" configuration is characterized by a filet-to-joint volume ratio of about 90% whereas the "nonoptimum" configuration has a lower ratio of about 75%. This gap, although not as wide as simulated, see Fig. 12, caused a decrease in the measured number of cycles to failure by a factor of 3 to 4. These results were obtained by continuous electrical monitoring tests. It confirms the predicted numerical trends and highlights the importance of the filet geometry.

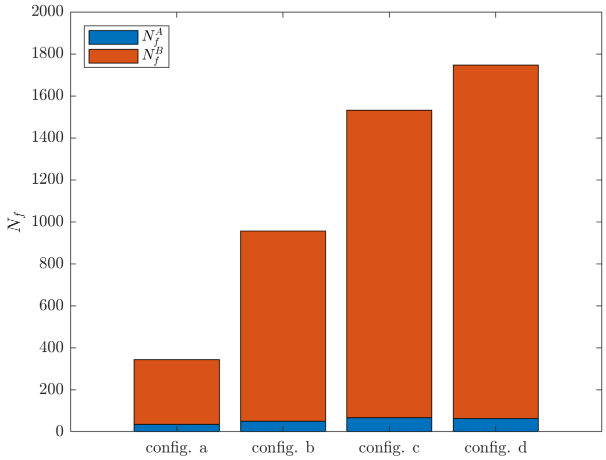

Fig. 13. Calculated number of cycles to failure in regions A and B for the four filet configurations presented in Fig. 12 based on the phenomenological failure models.

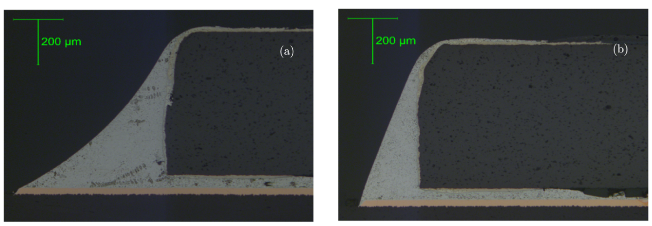

Fig. 14. Micrographs of the two filet geometries tested experimentally with (a) "optimum" design and (b) "nonoptimum" design.

B. Solder Joint Thickness Effect

Three normalized thicknesses are compared according to their lifetime in regions A and B in Fig. 15. The solder joint thickness is a first-order parameter in region A [5]. Indeed, from $t_{\text{solder}}/t_{\text{PCB}} = 7.5$ to $30 \cdot 10^{-3}$, N_f^A is increased by a factor 3. When changing $t_{\text{solder}}/t_{\text{PCB}}$ from 15 to $30 \cdot 10^{-3}$, the number of cycles to failure is doubled. But, once the number of cycles in region B is considered, the gap becomes much smaller; N_f^B substantially affects the total number of cycles. Lu et al. [35] also found that the thickness of the joint significantly affects N_f^A but, as the crack spends most of its time in region B to propagate, the shape and the volume of the filet play a more important role. As discussed previously, the volume used to calculate the inelastic strain energy is fixed and located at the border with region A. It means that the actual variations between the N_f^B are probably smaller than the calculated values. The influence of the solder joint thickness on the global number of cycles to failure is limited in the range of thicknesses calculated here. For thinner joints, N_f^A decreases to a very small number of cycles but as this only represents a tiny fraction of N_f, it only slightly impacts the global number of cycles. For thicker joints, N_f^A strongly increases and, hence, N_f also increases.

C. Component Size Effect

Three component sizes are presented in Fig. 16, from 1206 to 2512. The first two figures indicate the component length and the last two, the component width, both expressed in hundredths of inches. As expected, the larger the component, the shorter the lifetime. This trend is confirmed for both A and B regions. Like in Fig. 15, N_f^A is very small compared to N_f^B. It is more pronounced for larger components.

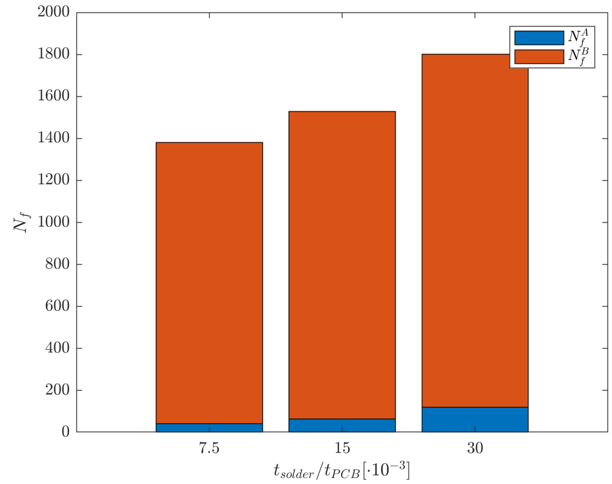

Fig. 15. Effect of the solder joint thickness on the number of cycles to failure in regions A and B.

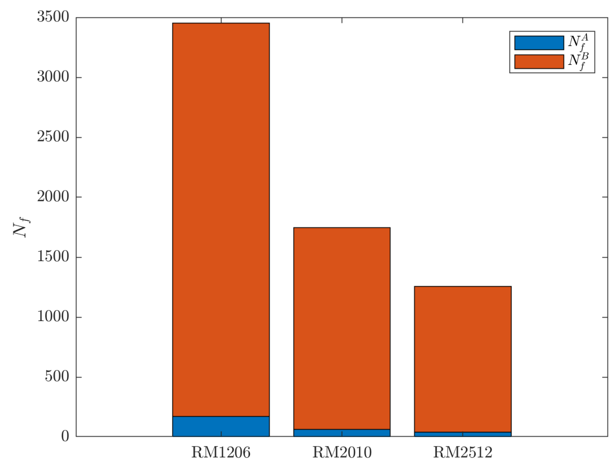

Fig. 16. Effect of the component size on the number of cycles to failure in regions A and B.

D. Temperature Cycle Effect

The temperature cycle is changed from −55 °C/100 °C at 10 °C/min to +20 °C/100 °C at 2 °C/min. The present model is compared to the widespread N-L aging law [36], see (4). The exponents and the subscripts 1 and 2 refer to temperature cycle conditions

$$N_f^2 = N_f^1 \left(\frac{\Delta T_1}{\Delta T_2}\right)^{1.9} \left(\frac{f_2}{f_1}\right)^{1/3} \times \exp\left(1414\left(\frac{1}{T_{\max,2}} - \frac{1}{T_{\max,1}}\right)\right) \quad (4)$$

where

f number of cycles per day;

$T_{\max}$ maximum temperature [K].

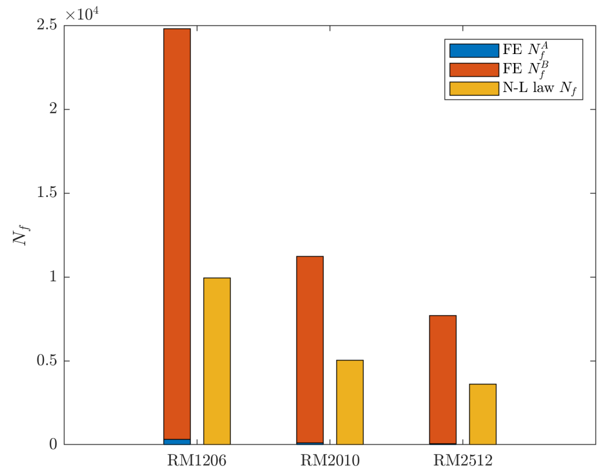

Fig. 17. Comparison between the two models developed for regions A and B and N-L aging law predictions, from results presented in Fig. 16 and for a temperature cycle from +20 °C to 100 °C at 2 °C/min.

Fig. 17 presents a comparison between the two approaches. Similar to Figs. 13–16, blue and red bars correspond to FE model predictions for regions A and B, respectively. Yellow bars refer to N-L aging law calculations from results presented in Fig. 16. Our predictions are more than two times higher. These results highlight the very conservative character of this law calling for more exploitation of our approach to be more predictive. Additional experimental work should be conducted to further assess the model predictions, especially with reduced temperature cycles.

IV. Conclusion

Two FE models have been developed, each based on a specific solder joint region, i.e., underneath the component and inside the filet. The model in region A uses a previously identified crack propagation model that relies on machine learning predictions, trained over a set of micro-section experimental results. A phenomenological failure law is identified and validated based on an inelastic strain energy criterion. The model in region B takes advantage of electrical monitoring experimental data and of the approach in region A to assess a phenomenological law, such as for region A. These FE simulations are conducted with a pre-crack underneath the component. The models are applied to several assembly configurations. This approach provides simple and convenient prediction capabilities. The contribution of the solder joint filet on the fatigue lifetime of the component assembly is explored. The main findings of this study are the following.

1) Region B and hence its shape and volume have a major contribution on the lifetime of the solder joint. The more extended the filet, the more damage resistance of the joint.
2) The effect of the joint thickness on the total number of cycles to failure is significantly mitigated compared to region A only where a decrease in thickness substantially reduces the lifetime.
3) The N-L aging law is used to estimate the lifetime of the assembly at another reduced temperature cycle and compared to the present model. The N-L aging law predictions were considerably lower highlighting its conservative character. This calls for more data generation and exploitation to establish and validate consistent model predictions.

Understanding the contribution of the filet in the thermomechanical fatigue of the joints allows a better assessment of the assembly's fatigue behavior. It also provides guidelines for new or optimized designs.

Acknowledgment

Computational resources have been provided by the supercomputing facilities of the Université catholique de Leuven (CISM/UCL) and the Consortium des Équipements de Calcul Intensif en Fédération Wallonie Brussels (CÉCI) funded by the Fond de la Recherche Scientifique de Belgique (F.R.S.-FNRS) under convention 2.5020.11 and by the Walloon Region.

References

[1] R. N. Wild, “Fatigue properties of solder joints,” Welding Res. Suppl., Welding Res. Council, pp. 521–526, Nov. 1972.
[2] R. Subrahmanyan, J. R. Wilcox, and C.-Y. Li, “A damage integral approach to thermal fatigue of solder joints,” *IEEE Trans. Compon., Hybrids, Manuf. Technol.*, vol. 12, no. 4, pp. 480–491, Dec. 1989.
[3] J. H. L. Pang, D. Y. R. Chong, and T. H. Low, “Thermal cycling analysis of flip-chip solder joint reliability,” *IEEE Trans. Compon. Packag. Technol.*, vol. 24, no. 4, pp. 705–712, Dec. 2001.
[4] L. Zhang, L. Sun, Y.-H. Guo, and C.-W. He, “Reliability of lead-free solder joints in CSP device under thermal cycling,” *J. Mater. Sci., Mater. Electron.*, vol. 25, no. 3, pp. 1209–1213, Mar. 2014.
[5] V. Voet, F. Van Loock, C. De Fruytier, A. Simar, and T. Pardoen, “Machine learning aided modelling of thermomechanical fatigue of solder joints in electronic component assemblies,” *Int. J. Fatigue*, vol. 167, Feb. 2023, Art. no. 107298.
[6] A. Syed, “Accumulated creep strain and energy density based thermal fatigue life prediction models for SnAgCu solder joints,” in *Proc. 54th Electron. Compon. Technol. Conf.*, vol. 1, Jun. 2004, pp. 737–746.
[7] L. Jiang, W. Zhu, and H. He, “Comparison of darveaux model and coffin-manson model for fatigue life prediction of BGA solder joints,” in *Proc. 18th Int. Conf. Electron. Packag. Technol. (ICEPT)*, Aug. 2017, pp. 1474–1477.
[8] X. Liu and G.-Q. Lu, “Effects of solder joint shape and height on thermal fatigue lifetime,” *IEEE Trans. Compon. Packag. Technol.*, vol. 26, no. 2, pp. 455–465, Jun. 2003.
[9] I. R. Holub, J. M. Pitarresi, and T. J. Singler, “Effect of solder joint geometry on the predicted fatigue life of BGA solder joints,” in *Proc. InterSociety Conf. Thermal Phenomena Electron. Syst., I-THERM V*, 1996, pp. 187–194.
[10] Q. Yu, M. Shiratori, and Y. Ohshima, “A study of the effects of BGA solder geometry on fatigue life and reliability assessment,” in *Proc. 6th Intersociety Conf. Thermal Thermomechanical Phenomena Electron. Syst. (ITherm)*, 1998, pp. 229–235.
[11] H.-T. Lee and K.-C. Huang, “Effect of solder-joint geometry on the low-cycle fatigue behavior of Sn-xAg-0.7 Cu,” *J. Electron. Mater.*, vol. 45, pp. 6102–6112, Jul. 2016.
[12] H. Wang, K. Pan, J. Ha, C. Cai, J. Xu, and S. Park, “The effect of solder paste volume on chip resistor solder joint fatigue life,” *Proc. Manuf.*, vol. 38, pp. 1372–1380, Jan. 2019.
[13] G. Zheng and C. Wang, “Shape and fatigue life prediction of chip resistor solder joints,” in *Proc. Int. Conf. Electron. Packag. Technol. High Density Packag.*, Aug. 2009, pp. 1167–1170.
[14] E. Jih and Y.-H. Pao, “Evaluation of design parameters for leadless chip resistors solder joints,” *J. Electron. Packag.*, vol. 117, no. 2, pp. 94–99, Jun. 1995.
[15] *Arlon 35n Polyimide Laminate and Prepreg*. Accessed: Apr. 26, 2022. [Online]. Available: https://www.arlonemd.com/wp-content/uploads/2020/04/35N.pdf
[16] W. D. Jenkins, T. G. Digges, and C. R. Johnson, “Tensile properties of copper, nickel, and 70-percent-copper-30-percent-nickel and 30-percent-copper-70-percentnickel alloys at high temperatures,” *J. Res. Nat. Bur. Standards*, vol. 58, pp. 201–211, Jun. 1957.

[17] G. Weber and L. Anand, “Finite deformation constitutive equations and a time integration procedure for isotropic, hyperelastic-viscoplastic solids,” *Comput. Methods Appl. Mech. Eng.*, vol. 79, no. 2, pp. 173–202, Mar. 1990.

[18] R. Darveaux, “Effect of simulation methodology on solder joint crack growth correlation and fatigue life prediction,” *J. Electron. Packag.*, vol. 124, no. 3, pp. 147–154, Sep. 2002.

[19] H. Tang and C. Basaran, “A damage mechanics-based fatigue life prediction model for solder joints,” *J. Electron. Packag.*, vol. 125, no. 1, pp. 120–125, Mar. 2003.

[20] A. Yeo, C. Lee, and J. H. L. Pang, “Flip chip solder joint reliability analysis using viscoplastic and elastic-plastic-creep constitutive models,” *IEEE Trans. Compon. Packag. Technol.*, vol. 29, no. 2, pp. 355–363, Jun. 2006.

[21] J. H. L. Pang, C. W. Seetoh, and Z. P. Wang, “CBGA solder joint reliability evaluation based on elastic-plastic-creep analysis,” *J. Electron. Packag.*, vol. 122, no. 3, pp. 255–261, Sep. 2000.

[22] C. Basaran and J. Jiang, “Measuring intrinsic elastic modulus of Pb/Sn solder alloys,” *Mech. Mater.*, vol. 34, no. 6, pp. 349–362, Jun. 2002.

[23] J.-P. Clech, “Solder reliability solutions: From LCCCs to area-array assemblies,” in *Proc. NEPCON WEST*, 1996, pp. 1665–1680.

[24] T.-Y. Hung, C.-J. Huang, C.-C. Lee, C.-C. Wang, K.-C. Lu, and K.-N. Chiang, “Investigation of solder crack behavior and fatigue life of the power module on different thermal cycling period,” *Microelectron. Eng.*, vol. 107, pp. 125–129, Jul. 2013.

[25] Y. Qi, R. Lam, H. R. Ghorbani, P. Snugovsky, and J. K. Spelt, “Temperature profile effects in accelerated thermal cycling of SnPb and Pb-free solder joints,” *Microelectron. Rel.*, vol. 46, nos. 2–4, pp. 574–588, Feb. 2006.

[26] R. Ghaffarian, “Effect of thermal cycling ramp rate on CSP assembly reliability,” in *Proc. 51st Electron. Compon. Technol. Conf.*, 2001, pp. 1170–1174.

[27] K.-C. Wu, S.-Y. Lin, T.-Y. Hung, and K.-N. Chiang, “Reliability assessment of packaging solder joints under different thermal cycle loading rates,” *IEEE Trans. Device Mater. Rel.*, vol. 15, no. 3, pp. 437–442, Sep. 2015.

[28] C. J. Zhai, Sidharth, and R. Blish, “Board level solder reliability versus ramp rate and dwell time during temperature cycling,” *IEEE Trans. Device Mater. Rel.*, vol. 3, no. 4, pp. 207–212, Dec. 2003.

[29] *High Reliability Assembly for Surface Mount and Through Hole Connections*, ECSS, Noordwijk, The Netherlands, 2022.

[30] X. Q. Shi, H. L. J. Pang, W. Zhou, and Z. P. Wang, “A modified energy-based low cycle fatigue model for eutectic solder alloy,” *Scripta Mater.*, vol. 41, no. 3, pp. 289–296, Jul. 1999.

[31] W. W. Lee, L. T. Nguyen, and G. S. Selvaduray, “Solder joint fatigue models: Review and applicability to chip scale packages,” *Microelectron. Rel.*, vol. 40, no. 2, pp. 231–244, Feb. 2000.

[32] S. Su, F. J. Akkara, R. Thaper, A. Alkhazali, M. Hamasha, and S. Hamasha, “A state-of-the-art review of fatigue life prediction models for solder joint,” *J. Electron. Packag.*, vol. 141, no. 4, Dec. 2019.

[33] H. Akay, H. Zhang, and N. Paydar, “Experimental correlations of an energy-based fatigue life prediction method for solder joints,” *Adv. Electron. Packag.*, vol. 2, pp. 1567–1574, Jan. 1997.

[34] W. Engelmaier, “Solder joints in electronics: Design for reliability,” in *Keynote Address in Design and Reliability of Solder and Solder Interconnectons*. Pittsburgh, PA, USA: The Minerals, Metals and Materials Society, 1997, pp. 9–19.

[35] H. Lu, C. Bailey, M. Dusek, C. Hunt, and J. Nottay, “Modelling the fatigue life of solder joints for surface mount resistors,” in *Proc. Int. Symp. Electron. Mater. Packag. (EMAP)*, 2000, pp. 136–142.

[36] K. C. Norris and A. H. Landzberg, “Reliability of controlled collapse interconnections,” *IBM J. Res. Develop.*, vol. 13, no. 3, pp. 266–271, May 1969.